

# Quantum control and process tomography of a semiconductor quantum dot hybrid qubit

Dohun Kim<sup>1</sup>, Zhan Shi<sup>1</sup>, C. B. Simmons<sup>1</sup>, D. R. Ward<sup>1</sup>, J. R. Prance<sup>1</sup>, Teck Seng Koh<sup>1</sup>, John King Gamble<sup>2</sup>, D. E. Savage<sup>3</sup>, M. G. Lagally<sup>3</sup>, Mark Friesen<sup>1</sup>, S. N. Coppersmith<sup>1</sup> & Mark A. Eriksson<sup>1</sup>

**The similarities between gated quantum dots and the transistors in modern microelectronics<sup>1,2</sup>—in fabrication methods, physical structure and voltage scales for manipulation—have led to great interest in the development of quantum bits (qubits) in semiconductor quantum dots<sup>3–18</sup>. Although quantum dot spin qubits have demonstrated long coherence times, their manipulation is often slower than desired for important future applications, such as factoring<sup>19</sup>. Furthermore, scalability and manufacturability are enhanced when qubits are as simple as possible. Previous work has increased the speed of spin qubit rotations by making use of integrated micromagnets<sup>11</sup>, dynamic pumping of nuclear spins<sup>12</sup> or the addition of a third quantum dot<sup>17</sup>. Here we demonstrate a qubit that is a hybrid of spin and charge. It is simple, requiring neither nuclear-state preparation nor micromagnets. Unlike previous double-dot qubits, the hybrid qubit enables fast rotations about two axes of the Bloch sphere. We demonstrate full control on the Bloch sphere with  $\pi$ -rotation times of less than 100 picoseconds in two orthogonal directions, which is more than an order of magnitude faster than any other double-dot qubit. The speed arises from the qubit's charge-like characteristics, and its spin-like features result in resistance to decoherence over a wide range of gate voltages. We achieve full process tomography in our electrically controlled semiconductor quantum dot qubit, extracting high fidelities of 85 per cent for  $X$  rotations (transitions between qubit states) and 94 per cent for  $Z$  rotations (phase accumulation between qubit states).**

As shown in Fig. 1a, the hybrid qubit<sup>20,21</sup> is formed in a double quantum dot in a Si/SiGe heterostructure<sup>22</sup>, with the gate voltages tuned so that two electrons occupy the left dot and one electron occupies the right dot (the (2, 1) charge state). Changing the voltage on gate L to make the energy difference  $\varepsilon$  between the quantum dots more positive favours a transition to the (1, 2) charge state. By changing  $\varepsilon$  adiabatically from positive to negative, we can track the qubit state  $|0\rangle \equiv |\downarrow\rangle|S\rangle$ , where  $S$  denotes a singlet state in the right dot, from right to left, as shown by the dark blue line in Fig. 1b. Similarly, the state  $|1\rangle \equiv 1/\sqrt{3}(|\downarrow\rangle|T_0\rangle + \sqrt{2/3}|\uparrow\rangle|T_-\rangle)$ , where  $T_0$  and  $T_-$  are two of the triplet states in the right dot, is shown by the magenta line in Fig. 1b.

The presence of the third electron in the pair of dots means that the states of the hybrid qubit are not purely singlet or triplet states, and we can therefore use fast electric field techniques to rotate the qubit about any axis of interest. In contrast, a two-electron singlet–triplet qubit requires slower, magnetic manipulation about one of the primary Bloch sphere axes. In addition, because the qubit is in only two dots rather than the three dots required for the exchange-only qubit<sup>16,17,23</sup>, the detuning  $\varepsilon$  is the only control parameter. The gate voltage space for controlling the qubit is thus one dimensional, making it straightforward to find ‘sweet spots’ where the decoherence effects of charge fluctuations on the qubit are greatly reduced. One of these sweet spots, at  $\varepsilon = 0$ , is the same as is found in a conventional charge qubit. The main difference between the hybrid qubit and a pure charge qubit is the presence of a very wide sweet spot at positive detuning  $\varepsilon \gg 0$ . In this regime, the detuning of the dot suppresses the exchange interaction, making the energy levels parallel as a

function of detuning, and providing strong protection against charge noise.

We first discuss data that demonstrates rotations of the qubit about two axes on the Bloch sphere. As shown schematically in Fig. 1c,  $X$  rotations on the Bloch sphere correspond to oscillations between qubit states  $|0\rangle$  and  $|1\rangle$ . To demonstrate such oscillations, we first prepare the qubit in state  $|0\rangle$ , by waiting for initialization at  $\varepsilon = \varepsilon_r$  (Fig. 1b). Changing the detuning abruptly to  $\varepsilon_x$  results in a Hamiltonian  $H = \mathcal{A}_1\sigma_x$ , where  $\sigma_x$  is the usual Pauli matrix and the tunnel coupling  $\mathcal{A}_1$  characterizes the strength of the anticrossing between  $|0\rangle$  and  $|1\rangle$ . Such a Hamiltonian is expected to result in oscillations between states  $|0\rangle$  and  $|1\rangle$  at the Larmor frequency  $2\mathcal{A}_1/h$ , where  $h$  is Planck's constant. The resulting final state is measured by changing the detuning to  $\varepsilon_r$ : at this detuning, the charge-sensing quantum point contact is used to determine whether the charge state is (2, 1), corresponding to state  $|0\rangle$ , or (1, 2) corresponding to state  $|1\rangle$  (see Methods Summary and Supplementary Information for details of the measurement procedure).

Figure 1e, f shows that this procedure results in rotations about the  $X$  axis of the Bloch sphere. In Fig. 1e we plot the probability  $P_0$  of observing state  $|0\rangle$  as a function of the pulse duration  $t_p$  and the gate voltage  $V_L$ , the latter of which determines  $\varepsilon$ . The path through Fig. 1e that corresponds to  $\varepsilon = 0$  is curved (Fig. 1e, dashed curve), because of frequency-dependent attenuation in the microwave coaxial cable<sup>24</sup>. Figure 1f shows a line cut through the path corresponding to  $\varepsilon = 0$ , revealing periodic oscillations in  $P_0$  at a frequency of 5.2 GHz, corresponding to  $\mathcal{A}_1/h \approx 2.6$  GHz. The visibility of this oscillation is larger than 0.8, and we estimate a lower bound for the coherence time of  $T_2^* \approx 2$  ns, by performing an exponential fit to the decay of the first 3 ns of the data. This  $X$  rotation alone is similar to a charge qubit rotation, and the coherence time is consistent with such an interpretation<sup>24–26</sup>. The most important parameter describing a quantum gate is the process fidelity; we return to this quantity below after demonstrating  $Z$  rotations, because two rotation axes are required for process tomography.

$Z$  rotations of the qubit, shown schematically in Fig. 1d as the orange line (Ramsey) about the equator of the Bloch sphere, can be performed by abruptly changing the detuning to a large, positive value,  $\varepsilon_z > 100 \mu\text{eV}$ . The states  $|0\rangle$  and  $|1\rangle$  have the same dependence on  $\varepsilon$  in this detuning range, differing in energy by a fixed value  $\delta E$  and creating a wide sweet spot that enables a controlled evolution of phase at a rate that is insensitive to fluctuations in  $\varepsilon$  arising, for example, from charge noise. Experimentally, the qubit is first prepared in state  $| - Y \rangle \equiv 1/\sqrt{2}(|0\rangle - i|1\rangle)$ , by initializing to state  $|0\rangle$  and performing an  $X(\pi/2)$  rotation, as described above. The resulting state can be rotated about the  $Z$  axis by setting the detuning equal to  $\varepsilon_z$  for a time  $t_p$ . We then measure the probability  $P_y$  of being in  $| Y \rangle \equiv 1/\sqrt{2}(|0\rangle + i|1\rangle)$ , by applying a second  $X(\pi/2)$  rotation to rotate this state into state  $|0\rangle$  and measuring the charge state at the readout position  $\varepsilon_r$  (see the orange inset to Fig. 1b). Figure 1g, h shows the resulting quantum oscillations of the qubit state around the  $Z$  axis of the Bloch sphere. The oscillations have a visibility larger than 0.85 and reveal a coherence time of  $T_2^* \approx 10$  ns, which is much longer than

<sup>1</sup>Department of Physics, University of Wisconsin-Madison, Madison, Wisconsin 53706, USA. <sup>2</sup>Sandia National Laboratories, Albuquerque, New Mexico 87185, USA. <sup>3</sup>Department of Materials Science and Engineering, University of Wisconsin-Madison, Madison, Wisconsin 53706, USA.

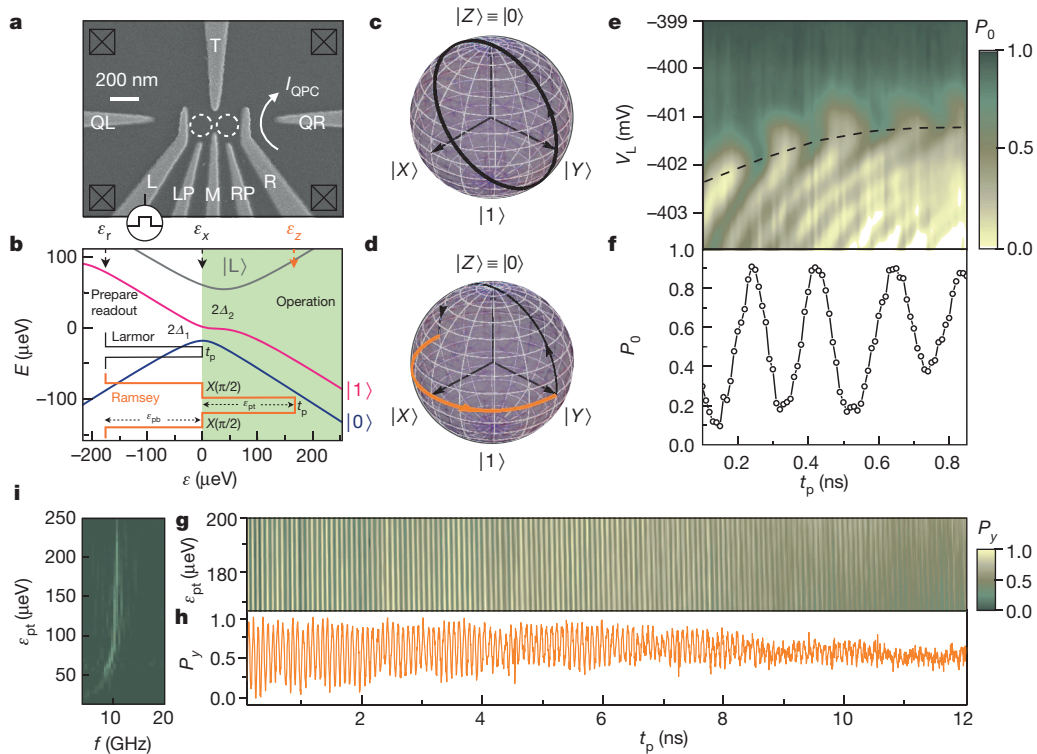


**Figure 1 | Si/SiGe hybrid qubit device, energy levels and measurement of quantum oscillations.** **a**, Scanning electron microscope image of a device lithographically identical to the one used in the experiment, with the locations of the double dot shown by white dashed circles. The current through the quantum point contact  $I_{\text{QPC}}$  is used for charge sensing via a measurement of its change in the presence of manipulation voltage pulses applied to gate L. The voltages on gates QL, QR, LP, M, RP and R are used to determine the overall operating point. **b**, Diagram of the calculated energy levels  $E$  versus detuning  $\varepsilon$ , including the ground states of the (2, 1) and (1, 2) charge configuration, the singlet–triplet splitting  $\delta E$  and the first excited state of the (1, 2) charge configuration, with Hamiltonian parameters determined as described in Supplementary Information. The resulting blue, magenta and grey solid curves show logical states  $|0\rangle$  and  $|1\rangle$  and the primary leakage state  $|L\rangle$ . Inset lines show pulse sequences used for implementation and measurement of rotations about the X axis (black) and Z axis (orange). **c**, **d**, Schematics of the evolution of the

the  $Z(\pi/2)$  manipulation time of approximately 25 ps. As is clear from the parallel fringes in Fig. 1g, the oscillation frequency does not depend on  $\varepsilon$ , resulting in the long  $T_2^*$ . As shown in Fig. 1i, we can quantify the width in  $\varepsilon$  of the sweet spot by performing a Fourier transform of similarly acquired Ramsey fringe data. The main peak in the transform corresponds to the Ramsey fringe frequency, which is nearly constant for  $\varepsilon_{\text{pt}} > 100 \mu\text{eV}$ , where  $\varepsilon_{\text{pt}}$  is the detuning energy at which the Ramsey phase accumulation occurs.

The initialization, measurement and two rotation gates just described enable full control of the qubit and provide the basis for tomographic characterization of the resulting qubit state. Figure 2a shows schematic diagrams of three pulse sequences that achieve this goal. For each of the three sequences, the qubit state is prepared in  $|0\rangle$  at  $\varepsilon_r$ , after which the detuning is pulsed to  $\varepsilon_x$  to perform an X rotation. By varying the time spent at  $\varepsilon_x$  from 160 to 340 ps—times that correspond to X rotation angles of approximately  $\pi$  to  $3\pi$ —the qubit at the end of the initialization sequence ('init' in Fig. 2a) can be set to a controlled and nearly arbitrary superposition of  $|0\rangle$  and  $|1\rangle$ . The limitation on this superposition is set by the X gate fidelity, which we extract below. In each of the three diagrams, this superposition state then evolves under a Z gate for a time  $t_p$ , reaching nearly all the rest of the Bloch sphere, with limitations again set by the Z gate fidelity.

Tomographic measurement is then performed by rotating the states  $|X\rangle \equiv 1/\sqrt{2}(|0\rangle + |1\rangle)$ ,  $|Y\rangle \equiv 1/\sqrt{2}(|0\rangle + i|1\rangle)$  and  $|Z\rangle \equiv |0\rangle$  into state

Bloch vector during pulse sequences for X-axis (**c**) and Z-axis (**d**) rotations. **e**, Probability  $P_0$  of the state to be  $|0\rangle$ , measured for the X-rotation pulse sequence as a function of the voltage  $V_L$  and pulse duration  $t_p$ . Dashed curve shows a path along  $\varepsilon \approx 0 \mu\text{eV}$ . **f**, Line cut of  $P_0$  along the dashed curve in **e**, as a function of  $t_p$ , starting at  $V_L \approx -402 \text{ mV}$  with pulse amplitude  $\varepsilon_{\text{pb}} \approx 160 \mu\text{eV}$ , showing  $\sim 5.2 \text{ GHz}$  quantum oscillations with coherence time  $T_2^* \approx 2 \text{ ns}$ . **g**, Probability  $P_y$  of the state being in  $|Y\rangle \equiv 1/\sqrt{2}(|0\rangle + i|1\rangle)$ , measured for the Z-rotation sequence as a function of pulse amplitude  $\varepsilon_{\text{pt}}$  and pulse duration  $t_p$  of the top pulse. Note the numerous parallel fringes, demonstrating that the frequency of Z rotation does not depend on  $\varepsilon_{\text{pt}}$ . **h**, Line cut of  $P_y$  as a function of  $t_p$  at  $\varepsilon_{\text{pt}} \approx 180 \mu\text{eV}$ , showing  $\sim 11.5 \text{ GHz}$  oscillations with coherence time  $T_2^* \approx 10 \text{ ns}$ . **i**, Fourier transform of Ramsey fringe data similar to that in **g**. The nearly vertical line at a frequency  $f \approx 11\text{--}12 \text{ GHz}$  corresponds to the Z-rotation frequency, indicating that the sweet spot extends for at least  $150 \mu\text{eV}$  in the upper two-thirds of the plot.

$|0\rangle$ , through the use of either a single X gate or a combination of an X gate and a Z gate, as shown by the blue lines in Fig. 2a. The resulting probability  $P_0$  is measured by pulsing the detuning back to  $\varepsilon_r$ . This initialization and measurement scheme provides universal control of the hybrid qubit and allows us to reconstruct fully the time evolution of the state vector.

As an example of control of the hybrid qubit, we perform Z rotations on the Bloch sphere starting with two different initial states. Figure 2b–d shows the probabilities  $P_x$ ,  $P_y$ , and  $P_z$  of measuring the system in the states  $|X\rangle$ ,  $|Y\rangle$  and  $|Z\rangle$  following a Z rotation with the initial state either close to  $|0\rangle$  (red data points) or close to  $| - Y\rangle$  (purple data points). In Fig. 2e, f we plot the Bloch vectors that are extracted from these three measurements for each time  $t_p$ . The results obtained are consistent with intuitive expectations: for input state  $|0\rangle$ , the time evolution under a Z rotation accumulates a trivial phase and the Bloch vector remains near the north pole of the Bloch sphere. For input state  $| - Y\rangle$ ,  $P_x$  and  $P_y$  oscillate sinusoidally between nearly 0 and 1, whereas  $P_z$  remains roughly constant with magnitude near 1/2, as expected.

Because the energy level structure of the qubit has been characterized experimentally, and the most likely leakage states are known (Fig. 1b), the rotation gates can be modelled numerically. The simulations incorporate realistic pulses with rise times of approximately 80 ps. The results of the calculations, shown as the solid orange ( $|0\rangle$  initialization) and solid purple ( $| - Y\rangle$  initialization) curves in Fig. 2b–f, are in good agreement

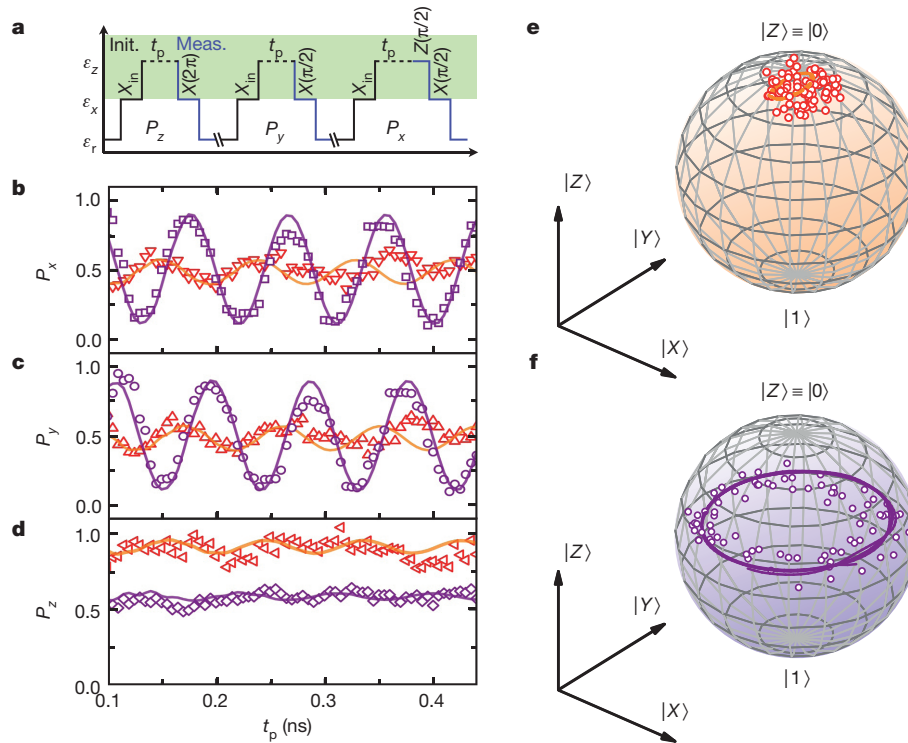


**Figure 2 | State tomography and universal gate control of the hybrid qubit.** **a**, Schematic diagrams of the pulse sequences used to perform state tomography by measuring the Z-axis projection  $P_z = P_0$ , the Y-axis projection  $P_y$ , and the X-axis projection  $P_x$  of the state that is initialized through an  $X_{in}$  gate and rotated around the Z axis for an evolution time  $t_p$ . **b–d**,  $P_x$ ,  $P_y$ , and  $P_z$  as functions of  $t_p$  for states initialized near  $|0\rangle$  (red symbols) and near  $|-Y\rangle \equiv 1/\sqrt{2}(|0\rangle - i|1\rangle)$  (purple symbols). Solid curves with corresponding colours are calculated from a model using non-adiabatic pulses with 80 ps rise times and the energy level diagram of Fig. 1a, with best-fit parameters

with the experiment. As we describe in Supplementary Information, leakage into state  $|L\rangle$  (shown in Fig. 1b) during these pulse sequences is 5% or less; in future work such leakage could be reduced further by appropriate pulse shaping. In Supplementary Information, we also report the results of an analogous state tomography of the qubit evolved under X rotations, using pulse sequences similar to those shown in Fig. 2a.

We now present quantum process tomography of the hybrid qubit. For a single qubit, the process matrix representation of any output state  $\mathcal{E}(\rho)$  for a given input state  $\rho$  resulting from a given quantum process can be written as<sup>27,28</sup>

$$\mathcal{E}(\rho) = \sum_{m,n=1}^4 \tilde{E}_m \rho \tilde{E}_n^\dagger \chi_{mn}$$

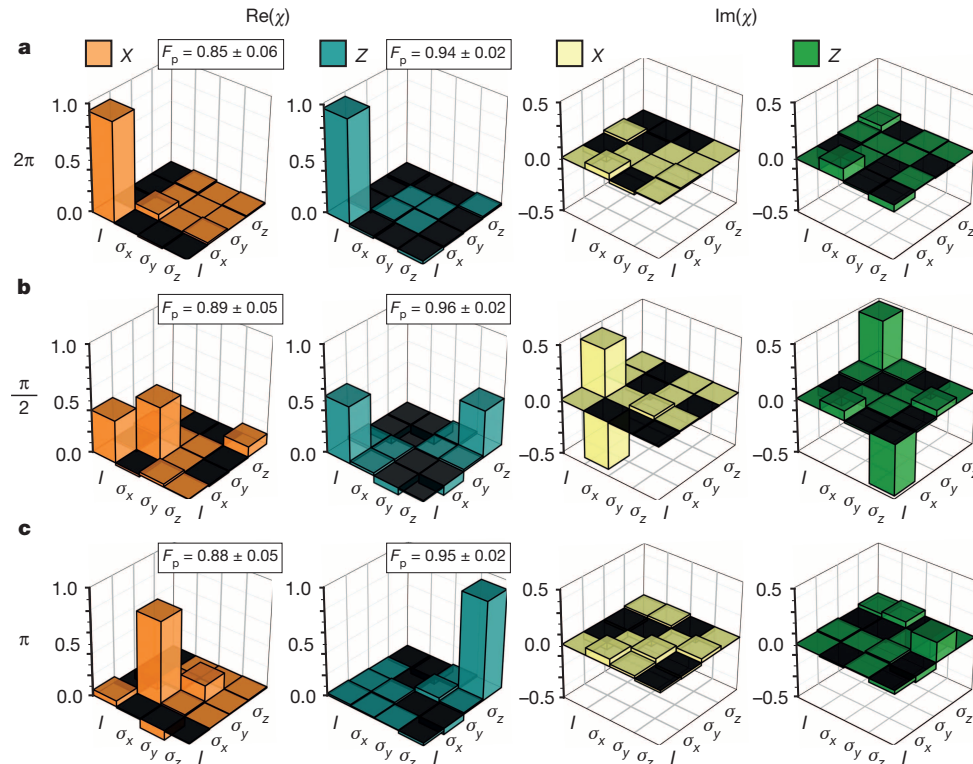
where the operators  $\tilde{E}_m$  form a basis in the space of  $2 \times 2$  matrices,  $\chi$  is the process matrix and a dagger denotes adjoint. To characterize both rotation axes, here we perform two sets of quantum process tomography: we consider both Z and X rotations, and for each we characterize rotations by an angle  $2\pi$  (nominally equivalent to zero rotation or the identity gate),  $\pi/2$  or  $\pi$ . To determine  $\chi_{mn}$  for each process, we prepare four linearly independent input and output states using the manipulation approach presented above and in Fig. 2a. The process matrix is then obtained using maximum-likelihood estimation<sup>27,28</sup>.

Figure 3 shows the results of this procedure; it reports in the Pauli basis  $\{I, \sigma_x, \sigma_y, \sigma_z\}$  the real and imaginary parts of  $\chi$  for both X and Z rotations of magnitude  $2\pi$ ,  $\pi/2$  or  $\pi$ . For each process, we find reasonably good agreement between the estimated process matrix  $\chi$  and the ideal process matrix  $\chi_{ideal}$ . The process fidelity is  $F_p = \text{Tr}(\chi_{ideal}\chi)$ , yielding  $F_p = 0.85 \pm 0.06$ ,  $0.89 \pm 0.05$  and  $0.88 \pm 0.05$  for the  $X(2\pi)$ ,  $X(\pi/2)$  and  $X(\pi)$  processes, respectively, and  $0.94 \pm 0.02$ ,  $0.96 \pm 0.02$  and  $0.95 \pm 0.02$  for the

$2A_1/h = 5.2$  GHz,  $2A_2/h = 14.8$  GHz and  $\delta E/h = 12.12$  GHz. The calculations neglect high-frequency dephasing but do include low-frequency fluctuations in the detuning  $\varepsilon$  (refs 23, 24 and Supplementary Information). **e**, Bloch sphere representation of the measured qubit state evolution under a Z gate that is initialized near  $|0\rangle$ . **f**, Representation with an input state near  $|-Y\rangle$ . Solid curves show the results of numerical simulations, as described above. The difference between **e** and **f** reflects the expected effect of Z rotations on the two different initial states.

$Z(2\pi)$ ,  $Z(\pi/2)$  and  $Z(\pi)$  processes. The statistical uncertainty is estimated using 30 different sets of input and output states for each process (see Supplementary Information for all the fidelity results for each set of input and output states).

The qubit studied here was formed in natural Si, in which the low density of nuclear spins has sufficient spin protection that spin dephasing does not limit coherence. Furthermore, the absence of piezoelectric coupling between electrons and phonons eliminates a dephasing channel that would be important in polar semiconductors<sup>29</sup>. With gate fidelities between 85% and 95%, the highest so far reported in an electrically gated semiconductor quantum dot qubit, the quantum dot hybrid qubit offers a promising combination of characteristics that in the past were found separately in qubits based on either charge or spin degrees of freedom: a good ratio of manipulation time to coherence time, together with fast overall operation and the ability to control the qubit fully using a single control parameter. It is important to emphasize the need for fast qubits: although the scaling associated with quantum computation is extremely promising for algorithms such as Shor's factoring algorithm and Grover's search algorithm, for the advantages to be realizable on time-scales relevant to humans, qubit operations must still be fast<sup>19</sup>. The fidelities of the X and Z gates reported here appear to be limited at present by the time spent in the regime near  $\varepsilon = 0$ , which is used for X rotations. In the future it may be possible to use a.c. driving of the control parameter to perform X rotations<sup>29</sup>, so that the regime in which the hybrid qubit is sensitive to charge noise may be avoided entirely. Even when the  $\varepsilon = 0$  regime is used for pulsed gating, as here, the hybrid qubit as demonstrated offers a desirable combination of high speed, high fidelity and efficient control in a semiconductor quantum dot qubit.



**Figure 3 | Quantum process tomography of the hybrid qubit.** Real and imaginary parts of the process matrix  $\chi$  obtained by maximum-likelihood estimation for three X- and Z-rotation processes in the Pauli basis ( $I, \sigma_x, \sigma_y, \sigma_z$ ). **a**, Rotation by  $2\pi$  (identity); **b**, rotation by  $\pi/2$ ; **c**, rotation by  $\pi$ . The measured process matrices are close to the targets for each operation; for example, the

target for an X( $\pi/2$ ) rotation is  $1/2$  for the ( $I, I$ ) and ( $\sigma_x, \sigma_x$ ) components,  $i/2$  and  $-i/2$  for the ( $I, \sigma_x$ ) and ( $\sigma_x, I$ ) components, respectively, and zero for all others. For each process, the average value and uncertainty of the process fidelity  $F_p = \text{Tr}(\chi_{\text{ideal}}\chi)$  is obtained from  $\chi$  for 30 distinct sets of input and output states (Supplementary Information).

## METHODS SUMMARY

**Measurement.** The experiments are performed on a three-electron double quantum dot fabricated in a Si/SiGe heterostructure<sup>22,25,26,30</sup> at base temperature (electron temperature,  $\sim 140$  mK; ref. 30) in a dilution refrigerator. Fast voltage pulses are generated by Agilent 81134A pulse generator and are added to the dot-defining d.c. voltage through a bias tee (Picosecond Pulselabs 5546-107) before being applied to gate L. The conductance change through the quantum point contact with and without the manipulation pulses, measured with a lock-in amplifier (EG&G model 7265), is used to determine the average charge occupation and is converted to the reported probabilities. To partially compensate pulse distortion due to frequency-dependent attenuation in coaxial cables, we developed a pulse correction scheme based on qubit rotation and measurement, which is applied to all the sequences shown in Fig. 2. In Supplementary Information, we present the details of the measurement technique, the probability normalization and the pulse correction scheme.

**Theory.** Numerical simulations of the experiment were performed on the basis of the energy level diagram in Fig. 1b. Parameters used in the simulation were extracted from experiment, as discussed in Supplementary Information. We model the dynamical evolution of the density matrix of the system as a function of detuning and pulse duration  $t_p$  using a master equation  $\dot{\rho} = -(i/\hbar)[H, \rho]$  with the Hamiltonian  $H$  written in a basis of the position eigenstates<sup>25,26</sup>. The ( $1, 2$ ) charge occupation probability is extracted at the end of the pulse and is averaged over 2 ns in the measurement stage of the pulse. Low-frequency fluctuations in the detuning  $\varepsilon$  are incorporated by convolving the simulation result<sup>24,25</sup> with a Gaussian distribution in  $\varepsilon$  of width  $\sigma_\varepsilon = 5 \mu\text{eV}$ .

Received 15 January; accepted 28 April 2014.

- Hanson, R., Kouwenhoven, L. P., Petta, J. R., Tarucha, S. & Vandersypen, L. M. K. Spins in few-electron quantum dots. *Rev. Mod. Phys.* **79**, 1217–1265 (2007).
- Zwanenburg, F. A. *et al.* Silicon quantum electronics. *Rev. Mod. Phys.* **85**, 961–1019 (2013).
- Loss, D. & DiVincenzo, D. P. Quantum computation with quantum dots. *Phys. Rev. A* **57**, 120–126 (1998).
- Hayashi, T., Fujisawa, T., Cheong, H. D., Jeong, Y. H. & Hirayama, Y. Coherent manipulation of electronic states in a double quantum dot. *Phys. Rev. Lett.* **91**, 226804 (2003).
- Petta, J. R., Johnson, A. C., Marcus, C. M., Hanson, M. P. & Gossard, A. C. Manipulation of a single charge in a double quantum dot. *Phys. Rev. Lett.* **93**, 186802 (2004).

- Elzerman, J. M. *et al.* Single-shot read-out of an individual electron spin in a quantum dot. *Nature* **430**, 431–435 (2004).
- Petta, J. R. *et al.* Coherent manipulation of coupled electron spins in semiconductor quantum dots. *Science* **309**, 2180–2184 (2005).
- Koppens, F. H. L. *et al.* Driven coherent oscillations of a single electron spin in a quantum dot. *Nature* **442**, 766–771 (2006).
- Kouwenhoven, L. P., Elzerman, J. M., Hanson, R., van Beveren, L. H. W. & Vandersypen, L. M. K. Control and measurement of electron spins in semiconductor quantum dots. *Phys. Stat. Solidi B* **243**, 3682–3691 (2006).
- Taylor, J. M. *et al.* Relaxation, dephasing, and quantum control of electron spins in double quantum dots. *Phys. Rev. B* **76**, 035315 (2007).
- Pioro-Ladrière, M. *et al.* Electrically driven single-electron spin resonance in a slanting Zeeman field. *Nature Phys.* **4**, 776–779 (2008).
- Foletti, S., Bluhm, H., Mahalu, D., Umansky, V. & Yacoby, A. Universal quantum control of two-electron spin quantum bits using dynamic nuclear polarization. *Nature Phys.* **5**, 903–908 (2009).
- Laird, E. A. *et al.* Coherent spin manipulation in an exchange-only qubit. *Phys. Rev. B* **82**, 075403 (2010).
- Gaudreau, L. *et al.* Coherent control of three-spin states in a triple quantum dot. *Nature Phys.* **8**, 54–58 (2012).
- Maune, B. M. *et al.* Coherent singlet-triplet oscillations in a silicon-based double quantum dot. *Nature* **481**, 344–347 (2012).
- Medford, J. *et al.* Quantum-dot-based resonant exchange qubit. *Phys. Rev. Lett.* **111**, 050501 (2013).
- Medford, J. *et al.* Self-consistent measurement and state tomography of an exchange-only spin qubit. *Nature Nanotechnol.* **8**, 654–659 (2013).
- Dial, O. E. *et al.* Charge noise spectroscopy using coherent exchange oscillations in a singlet-triplet qubit. *Phys. Rev. Lett.* **110**, 146804 (2013).
- Van Meter, R., Itoh, K. M. & Ladd, T. D. in *Controllable Quantum States: Mesoscopic Superconductivity & Spintronics (MS+S2006)*, Proc. Int. Symp. (eds Takayanagi, H., Nitta, J. & Nakano, H.) 183–188 (World Scientific, 2008); preprint at <http://arxiv.org/abs/quant-ph/0507023> (2006).
- Shi, Z. *et al.* Fast hybrid silicon double quantum dot qubit. *Phys. Rev. Lett.* **108**, 140503 (2012).
- Koh, T. S., Gamble, J. K., Friesen, M., Eriksson, M. A. & Coppersmith, S. N. Pulse-gated quantum dot hybrid qubit. *Phys. Rev. Lett.* **109**, 250503 (2012).
- Thalakulam, M. *et al.* Fast tunnel rates in Si/SiGe one-electron single and double quantum dots. *Appl. Phys. Lett.* **96**, 183104 (2010).
- DiVincenzo, D. P., Bacon, D., Kempe, J., Burkard, G. & Whaley, K. B. Universal quantum computation with the exchange interaction. *Nature* **408**, 339–342 (2000).
- Petersson, K. D., Petta, J. R., Lu, H. & Gossard, A. C. Quantum coherence in a one-electron semiconductor charge qubit. *Phys. Rev. Lett.* **105**, 246804 (2010).

25. Shi, Z. *et al.* Coherent quantum oscillations and echo measurements of a Si charge qubit. *Phys. Rev. B* **88**, 075416 (2013).
26. Shi, Z. *et al.* Fast coherent manipulation of three-electron states in a double quantum dot. *Nature Commun.* **5**, 3020 (2014).
27. Nielsen, M. A. & Chuang, I. L. *Quantum Computation and Quantum Information* 389–393 (Cambridge Univ. Press, 2000).
28. Chow, J. M. *et al.* Randomized benchmarking and process tomography for gate errors in a solid-state qubit. *Phys. Rev. Lett.* **102**, 090502 (2009).
29. Koh, T. S., Coppersmith, S. N. & Friesen, M. High-fidelity gates in quantum dot spin qubits. *Proc. Natl Acad. Sci. USA* **110**, 19695–19700 (2013).
30. Simmons, C. B. *et al.* Tunable spin loading and  $T_1$  of a silicon spin qubit measured by single-shot readout. *Phys. Rev. Lett.* **106**, 156804 (2011).

**Supplementary Information** is available in the online version of the paper.

**Acknowledgements** This work was supported in part by ARO (W911NF-12-0607), the NSF (PHY-1104660) and by the Laboratory Directed Research and Development programme at Sandia National Laboratories. Sandia National Laboratories is a multi-programme laboratory managed and operated by Sandia Corporation, a wholly

owned subsidiary of Lockheed Martin Corporation, for the US Department of Energy's National Nuclear Security Administration under contract DE-AC04-94AL85000. Development and maintenance of the growth facilities used for fabricating samples is supported by the US Department of Energy (DE-FG02-03ER46028). This research used US National Science Foundation-supported shared facilities at the University of Wisconsin-Madison. D.K. acknowledges conversations with X. Wu and K. Rudinger.

**Author Contributions** M.A.E. and S.N.C. had the idea for the experiment. D.K. developed pulse sequences for qubit operation and tomography, performed electrical measurements and numerical simulations with the aid of Z.S., and analysed the data with M.A.E. and S.N.C. C.B.S. fabricated the quantum dot device. J.R.P. and D.R.W. developed hardware and software for the measurements. T.S.K., J.K.G. and M.F. helped with the theoretical analysis. D.E.S. and M.G.L. prepared the Si/SiGe heterostructure. D.K., S.N.C. and M.A.E. wrote the manuscript with the contributions of all authors.

**Author Information** Reprints and permissions information is available at [www.nature.com/reprints](http://www.nature.com/reprints). The authors declare no competing financial interests. Readers are welcome to comment on the online version of the paper. Correspondence and requests for materials should be addressed to M.A.E. ([maeriksson@wisc.edu](mailto:maeriksson@wisc.edu)).